



## Targeted synthesis of visible-light-driven covalent organic framework photocatalyst via molecular design and precise construction



Sijing He<sup>a,b</sup>, Bing Yin<sup>c</sup>, Hongyun Niu<sup>a</sup>, Yaqi Cai<sup>a,b,d,\*</sup>

<sup>a</sup> State Key Laboratory of Environmental Chemistry and Ecotoxicology, Research Center for Eco-Environmental Sciences, Chinese Academy of Sciences, Beijing 100085, China

<sup>b</sup> University of Chinese Academy of Sciences, Beijing 100049, China

<sup>c</sup> Key Laboratory of Synthetic and Natural Functional Molecule, Chemistry of Ministry of Education, College of Chemistry and Materials Science, Northwest University, Xi'an 710127, China

<sup>d</sup> Institute of Environment and Health, Jianghan University, Wuhan 430056, China

### ARTICLE INFO

#### Keywords:

Covalent organic frameworks  
Molecular engineering  
Tunable band structure  
Visible-light-driven  
Photocatalysis

### ABSTRACT

Given the structural diversity and tailorability, covalent organic frameworks (COFs) were regarded as an appealing platform for the molecular design of organic semiconductors. The band structure and physicochemical properties can be easily tuned by tailoring the building blocks. Here we synthesized a series of imine-linked COFs from the same aldehyde and three different monomers of nitrogen-containing functional groups, and investigated the translation of chemical and structural variation in the precursors to photoelectric properties of the resulting COFs, with the consequent influence on photocatalytic degradation. We found that the visible-light photocatalytic performances were enhanced with increasing density of active centers and conjugation degree in the networks, which provide a forceful basis for the systematic fine-tuning of their structural and physicochemical properties thus broadening the applications of COFs in photocatalysis.

### 1. Introduction

Covalent organic frameworks (COFs) are an emerging type of crystalline porous polymers that enable atomically precise integration of organic subunits into predetermined skeletons [1–6]. Owing to the structural and compositional diversity of building blocks, COFs offer a versatile platform to the designed synthesis of advanced organic materials that are promising for handling environmental issues. Visible-light-induced photocatalyst can directly harvest sunlight as a clean and renewable source to alleviate global energy and environment crisis [7,8]. The crucial difficulty of the field lies in the pursuit of efficient and sustainable candidates with high visible-light response. Graphitic carbon nitride ( $\text{g-C}_3\text{N}_4$ ), as a metal-free organic semiconductor material, has attracted great interest due to its desirable band gap (2.70 eV). However, the downsides of marginal visible-light absorption and fast charge recombination severely hamper its wide applications. In addition,  $\text{g-C}_3\text{N}_4$  only composed of heptazine or triazine units, thus offering limited chemical variations for structural optimization. Thanks to the inherent merits of high specific surface area, tunable pore size and structure, and facilely-tailored functionality, pure COFs materials hold

great potential in it [9–12]. However, the research effort in this respect is far from adequate. More recently, we successfully constructed a superior visible-light-responsive photocatalyst based on a  $\text{C}_3\text{N}_4$  active centre-photoelectron shift platform-electron withdrawing unit triadic structure COFs [13]. It possesses ultrahigh photodegradation efficiency, far outperforming the bulk graphitic carbon nitride ( $\text{g-C}_3\text{N}_4$ ).

Generally, the development of a novel type of photocatalyst needs to be screened by extensive experiment which is time-consuming and less effective. Nevertheless, progress over the past decade in photocatalysis has gradually introduced the concept of controllability to the design philosophy of photocatalyst [14–19], which made the preparation process more directive and efficient. The rich variation of the constituting building units opens enormous possibilities to regulate COFs structures, therefore it seems to be an ideal molecular template to meet the demand of controllability. The performance of the photocatalyst is mainly determined by its intrinsic energy band structure and the separation of photogenerated charge carriers. To establish the structure-properties relationship between COFs molecular configuration and its photocatalytic activity is of great significance to develop new potent photocatalyst. Based on above analysis, we altered COFs

\* Corresponding author at: State Key Laboratory of Environmental Chemistry and Ecotoxicology, Research Center for Eco-Environmental Sciences, Chinese Academy of Sciences, Beijing 100085, China.

E-mail address: [caiyqi@rcees.ac.cn](mailto:caiyqi@rcees.ac.cn) (Y. Cai).

architectures to tune light harvesting and maneuver charge kinetic, in order to further explore the structural factors that impact the photocatalytic efficiency.

Herein, three COFs bearing visible-light catalytic active substituent of triazine ring were employed as metal-free and visible-light-active photocatalysts for contaminant degradation. We precisely adjusted COFs structures by assembling the diverse building units, and then further analyzed the relationship between the structure, physicochemical properties and photocatalytic performance of photocatalyst. Our results suggest that the density of active centers and the conjugation degree in the frameworks are intimately correlated with the charge generation and recombination kinetics, thus dramatically affecting the photocatalytic capacity. As expected, the  $\text{COF}_{\text{A}+\text{C}}$  with richly available active sites and highly delocalized  $\pi$ -system exhibited superb photocatalytic activity in eliminating organic pollutant under visible light. Additionally, these COFs photocatalysts are fairly stable even after repeated cycling. The performance of materials can be traced by the origin of their chemical structures, in turn, the desired materials are expected to acquire via predesigning their molecular structure.

## 2. Experimental

### 2.1. Synthesis of $\text{COF}_{\text{A}+\text{B}}$ , $\text{COF}_{\text{A}+\text{C}}$ and $\text{COF}_{\text{A}+\text{D}}$

4,4',4''-(1,3,5-Triazine-2,4,6-triyl)tribenzaldehyde (**A**) (0.25 mmol, 98.3 mg) and either 1,3,5-tris(4-aminophenyl)benzene (**B**) (for  $\text{COF}_{\text{A}+\text{B}}$ ), 4,4',4''-(1,3,5-triazine-2,4,6-triyl)trianiline (**C**) (for  $\text{COF}_{\text{A}+\text{C}}$ ), or 2,4,6-tris(4-hydrazinylphenyl)-1,3,5-triazine (**D**) (for  $\text{COF}_{\text{A}+\text{D}}$ ) (0.25 mmol) were dissolved in a ternary solvent mixture of mesitylene/1,4-dioxane/3 M acetic acid (5/5/1 by vol.; 11.0 mL). The reaction mixture was sonicated for 15 min, bubbled with  $\text{N}_2$  for another 15 min, and then heated at 120 °C for 3 days. After being cooled to room temperature, the precipitate was washed with acetone and THF, and then dried under vacuum at 120 °C for 10 h. Finally,  $\text{COF}_{\text{A}+\text{B}}$ ,  $\text{COF}_{\text{A}+\text{C}}$  and  $\text{COF}_{\text{A}+\text{D}}$  were obtained as ochre-yellow, pale-yellow, and orange powders, respectively.

### 2.2. Characterization

The morphology of the synthesized photocatalysts was characterized by a Hitachi H-7500 transmission electron microscope (TEM, Tokyo, Japan). Powder X-ray diffraction (PXRD, Almelo, Netherlands) using a Cu K $\alpha$  radiation ranging from 3° to 60° with a resolution of 0.02° was utilized to analysis the crystalline. Fourier transform-infrared (FT-IR) spectra in the 4000–400  $\text{cm}^{-1}$  region were recorded on a NEXUS 670 Infrared Fourier Transform Spectrometer (Nicolet Thermo, Waltham, MA). Solid-state nuclear magnetic resonance (NMR) spectroscopy was obtained on a JNM-ECZ600R spectrometer (JEOL). Elemental analysis (EA) was conducted on an EA3000 analyzer (EURECTOR). Thermogravimetric analysis (TGA) was carried out on a TGA Q5000 IR thermogravimetric analyzer (TA Instruments, New Castle, U.S.A.) with the heating rate of 10 °C  $\text{min}^{-1}$  under  $\text{N}_2$  atmosphere. Surface area and pore volume were measured by Brunauer–Emmett–Teller (BET) methods (ASAP2000 V3.01A; Micrometrics, Norcross, GA). The diffuse reflectance spectra (DRS) were collected using a Hitachi U-3900 UV-vis spectrophotometer ( $\text{BaSO}_4$  as a reflectance standard). All contact angles were measured on the OCA20 Contact Angle Measuring System (Dataphysics). Surface analysis by X-ray photoelectron spectroscopy (XPS) was carried out using Thermo Fisher ESCALAB 250Xi equipment (Waltham, MA), and the X-ray source was Al K $\alpha$  radiation (1486.6 eV, monochromatic). The photoluminescence (PL) spectra of samples were detected on an FS5 fluorescence spectrometer (Edinburgh Instruments, England). All the electrochemical properties were investigated on a CHI660E electrochemical analyzer (Chenhua, Shanghai, China) in a standard three-electrode system, using a platinum foil as the counter electrode and Ag/AgCl

(saturated KCl) as the reference electrode. The electrolyte was a 0.1 mol  $\text{L}^{-1}$   $\text{Na}_2\text{SO}_4$  aqueous solution. The working electrodes were prepared as follows: 5 mg of photocatalyst powder was dispersed in 0.5 mL of DMF, which was dip-coated on the surface of indium tin oxide (ITO) glass substrate. Subsequently, 5% Nafion-ethanol solution was dripped onto the sample film and dried at 100 °C. Mott-Schottky curves were measured at a frequency of 1 kHz. The EIS frequency ranged from 10 m to 100 kHz with an AC voltage magnitude of 10 mV. Visible-light irradiation was provided by a CEL-HXF300F3 300 W xenon lamp (CEAU-LIGHT) with a 420 nm cut-off filter.

### 2.3. Photocatalytic activity measurements

The photocatalytic activities of the as-synthesized samples were evaluated by degradation of methyl orange (MO) and phenol under visible light irradiation. The visible light source was a 300 W xenon lamp equipped with an optical cutoff filter ( $\lambda \geq 420$  nm). Typically, 15 mg of the photocatalyst powder was dispersed into 50 mL organic pollutant solution with a concentration of 10  $\text{mg L}^{-1}$ . Prior to light illumination, the suspension was magnetically stirred for 1 h in the dark to reach an adsorption–desorption equilibrium. At the given intervals, 3 mL of aliquot was extracted and centrifuged to remove the photocatalyst. After that, the resulting supernatants were analyzed by monitoring the absorbance spectra on a UV-vis spectrophotometer. The mineralization of MO under different irradiation times was studied by a total organic carbon (TOC) analyzer (SHIMADZU).

## 3. Results and discussion

The precursors 4,4',4''-(1,3,5-triazine-2,4,6-triyl)tribenzaldehyde (**A**) and 2,4,6-tris(4-hydrazinylphenyl)-1,3,5-triazine (**D**) were synthesized as described in the Supporting information, and they were characterized using  $^1\text{H}$  NMR and mass spectroscopy. Three imine-based COFs (denoted as  $\text{COF}_{\text{A}+\text{B}}$ ,  $\text{COF}_{\text{A}+\text{C}}$  and  $\text{COF}_{\text{A}+\text{D}}$ ) were successfully synthesized under solvothermal conditions via co-condensation of 4,4',4''-(1,3,5-triazine-2,4,6-triyl)tribenzaldehyde (**A**) and either 1,3,5-tris(4-aminophenyl)benzene (**B**), 4,4',4''-(1,3,5-triazine-2,4,6-triyl)trianiline (**C**), or 2,4,6-tris(4-hydrazinylphenyl)-1,3,5-triazine (**D**). As illustrated in Fig. 1, the dehydrations of aldehyde and amino groups give rise to the Schiff-base type linkages.

The chemical identity of the resulting powders was initially confirmed by elemental analysis, Fourier transform infrared (FT-IR) spectroscopy, and solid-state  $^{13}\text{C}$  cross-polarization magic angle spinning nuclear magnetic resonance (CP-MAS NMR) spectroscopy. Elemental analysis of three samples corroborates well with the theoretical values of infinite 2D sheet (Table S1). FT-IR spectra of  $\text{COF}_{\text{A}+\text{B}}$ ,  $\text{COF}_{\text{A}+\text{C}}$  and  $\text{COF}_{\text{A}+\text{D}}$  were compared with the starting materials (Fig. S7 in the Supporting information). As shown, the characteristic C=O (1706  $\text{cm}^{-1}$ ) and aldehydic C–H (2819 and 2729  $\text{cm}^{-1}$ ) stretching bands disappeared with the concomitant appearance of the imine (C=N) stretching vibrational bands at 1612  $\text{cm}^{-1}$  for  $\text{COF}_{\text{A}+\text{B}}$ , 1607  $\text{cm}^{-1}$  for  $\text{COF}_{\text{A}+\text{C}}$ , and 1608  $\text{cm}^{-1}$  for  $\text{COF}_{\text{A}+\text{D}}$ , indicative of the consumption of the aldehydes and the completion of the condensations. The  $^{13}\text{C}$  CP-MAS NMR spectra of all COFs displayed the characteristic resonance signals at 156–159 ppm assignable to the C=N carbon (Fig. 2a), suggesting the conversion of the precursors into the respective COFs. The molecular structure of the building units remains intact during COFs formation as evident by the characteristic peaks at about 170 ppm for the central triazine ring. X-ray photoelectron spectroscopy (XPS) also verified the formation of the expected imine linkages in these three COFs. In high resolution N 1s spectra, the peak-area ratios of N–H to C=N–C in the three precursors shows an obvious decrease with respect to the corresponding of COFs, suggesting the lost portion of amine groups and the increased portion of imine groups (Fig. S8). Transmission electron microscopy (TEM) images showed a long thread-like morphology (Fig. 2b–d). Besides, only  $\text{COF}_{\text{A}+\text{C}}$  sprouted the thorn-like

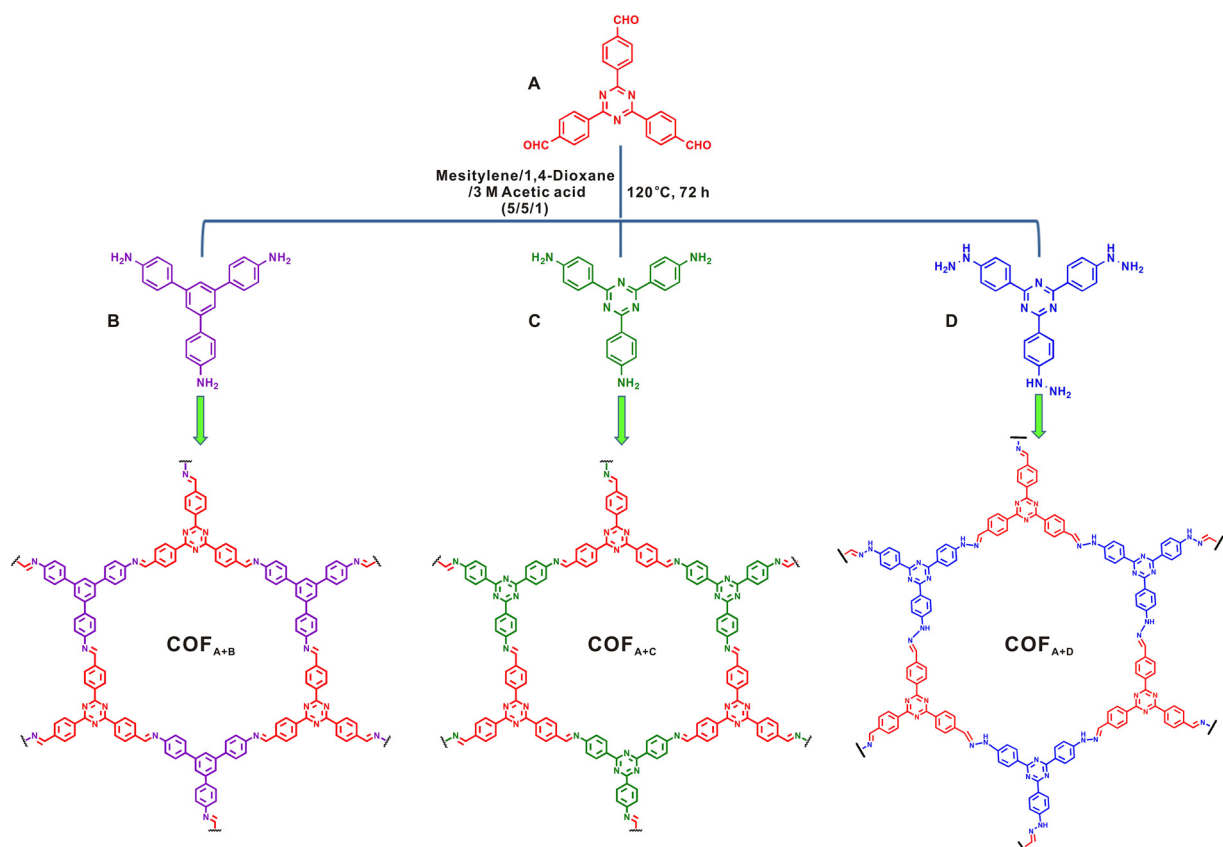


**Fig. 1.** Synthesis of covalent organic frameworks via Schiff-base chemistry of different nitrogen-containing building blocks with 4,4',4''-(1,3,5-triazine-2,4,6-triyl)tribenzaldehyde.

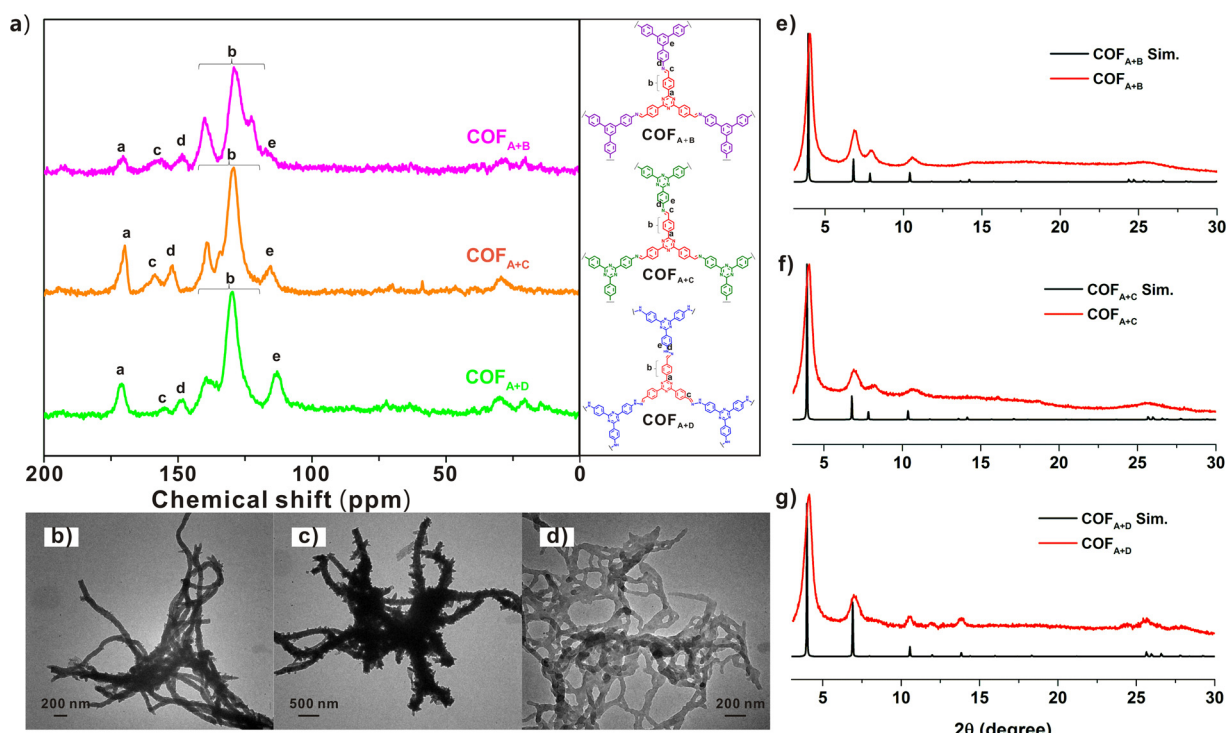


**Fig. 2.** (a) Comparison of the <sup>13</sup>C CP-MAS solid-state NMR spectra of COF<sub>A+B</sub>, COF<sub>A+C</sub>, and COF<sub>A+D</sub>; TEM images of (b) COF<sub>A+B</sub>, (c) COF<sub>A+C</sub>, and (d) COF<sub>A+D</sub>; PXRD patterns of (e) COF<sub>A+B</sub>, (f) COF<sub>A+C</sub>, and (g) COF<sub>A+D</sub>. Experimental and simulated patterns are in red and black, respectively. (For interpretation of the references to color in this figure legend, the reader is referred to the web version of this article).

structure (Fig. 2c), which results in a larger specific surface area with more accessible active sites. All of the COFs have almost identical thermal stabilities up to around 300 °C under a nitrogen atmosphere (Fig. S9), as revealed by thermal gravimetric analysis (TGA).

The crystallinity of all the COFs was resolved by Powder X-ray diffraction (PXRD) analysis with Cu K $\alpha$  radiation. Structural modelling was conducted with the Materials Studio (ver. 6.0) suit of program. Comparison of the experimental and the calculated PXRD patterns indicated that the preferred stacking structure of all these COFs were the eclipsed arrangements (Figs. 2e–g and S10–S12). The highly crystalline nature of these COFs contributes to enhancing the charge mobility [20]. The permanent porosities of COFs were assessed by measuring nitrogen adsorption isotherms at 77 K. As can be seen in Fig. S13, all the COFs showed typical type-IV isotherms, which are characteristic of mesoporous materials. The Brunauer–Emmett–Teller (BET) surface areas of the three COFs were found to be 907 (COF<sub>A+B</sub>), 1903 (COF<sub>A+C</sub>), and 458 m<sup>2</sup> g<sup>-1</sup> (COF<sub>A+D</sub>), with total pore volumes of 0.436, 0.455, and 0.434 cm<sup>3</sup> g<sup>-1</sup>, respectively. Their accessible porous nature with a large surface area is conducive to mass transfer [21,22].

The release of colored wastes such as dyes from industry to the ecosystem is highly toxic to aquatic life and causes serious threat to the environment. Methyl orange (MO, an azo dye) is considerably stable under visible light exposure in the absence of a photocatalyst, and the self-photolysis can be negligible. Here, we chose MO dye and colorless phenol as model contaminants to assess the photocatalytic activities of the obtained COFs. Prior to any photocatalytic tests, dark absorption tests were conducted by putting photocatalysts into contact with target pollutants without illumination. As can be seen, these three polymers showed different adsorption abilities towards MO and phenol. In general, the increases in surface area and pore volume accompanied with more available active sites for adsorption could result in enhanced adsorption ability. Simultaneously, however, the structures of polymers substantially impact the adsorbent-adsorbate affinity. By analyzing of the chemical structures of COFs and adsorbates, we attempt to offer a more plausible explanation. As MO was adsorbed on polymers mainly via  $\pi$ – $\pi$  stacking interaction, a larger quantity of benzene rings in the skeleton of polymer endows COF<sub>A+B</sub> with a higher adsorption capacity for MO. Moreover, the azo groups ( $=N=N-$ ) of MO could interact with hydrazine groups on COF<sub>A+D</sub> through H-bonding, which makes its adsorption activity superior to COF<sub>A+C</sub>. The adsorption of phenol was attributed to the formation of H-bonding between hydroxyl groups of phenol and N-containing functional groups on polymers. Among them, the sequence of the proportions of nitrogen atom which can form H-bonding in the frameworks is COF<sub>A+C</sub> > COF<sub>A+D</sub> > COF<sub>A+B</sub>. Accordingly, the adsorption of MO on polymers followed the order of COF<sub>A+B</sub> > COF<sub>A+D</sub> > COF<sub>A+C</sub>, whereas the adsorption affinity of phenol decreased in the order COF<sub>A+C</sub> > COF<sub>A+D</sub> > COF<sub>A+B</sub>.

The visible-light-responsive photocatalytic performances of the samples were evaluated by measuring the decomposition rate of the model contaminants under visible light irradiation (Fig. 3a). Surprisingly, such slight structural differences of these three polymers led to an enormous discrepancy in the photocatalytic activities. It can be seen that COF<sub>A+C</sub> exhibits superior MO photodegradation capacity compared with its analogues COF<sub>A+B</sub> and COF<sub>A+D</sub>. After 30 min irradiation with visible light, COF<sub>A+C</sub> could completely degrade MO molecules (Fig. 3b), whereas only 29.6% MO was removed by COF<sub>A+B</sub>. Meanwhile, almost no decolorization of MO was observed in the presence of COF<sub>A+D</sub>. In general, the photocatalytic decomposition of MO obeys pseudo-first-order kinetics, that is,  $-\ln(C/C_0) = kt$ , where C<sub>0</sub> and C are the initial and actual concentrations of MO, respectively, and k is the kinetic constant. From Fig. 3c, it is clearly presented that COF<sub>A+C</sub> possesses highest photodegradation efficiency with an apparent rate constant of 0.09 min<sup>-1</sup>, which is above 2 times higher than that of COF<sub>A+B</sub> (0.04 min<sup>-1</sup>). This may be ascribed to the higher density of visible-light active centers (triazine ring) in the framework of COF<sub>A+C</sub>. With optimum photocatalyst COF<sub>A+C</sub>, 25.6% of mineralization of MO is

reached after illumination for 30 min. As shown in Fig. 3d, similar photocatalytic degradation trends are achieved with phenol: 79.0% of phenol was decomposed with COF<sub>A+C</sub> after 30 min under visible light irradiation, compared to only 46.6% and 6.4% with COF<sub>A+B</sub> and COF<sub>A+D</sub>, respectively.

To better understand the origin of their significant differences in photocatalytic efficiency, it is necessary to deeply investigate their optical and electronic properties. Fig. 4a shows the optical properties of three as-prepared COFs, as measured by UV-vis diffuse reflectance spectra (DRS). It is evident that the selection of different building blocks changes the colors of polymers from pale yellow to orange (inset in Fig. 3a), implying increased absorption in the visible light region. The band gap energies (E<sub>g</sub>) are estimated to be 2.49, 2.56 and 2.21 eV for COF<sub>A+B</sub>, COF<sub>A+C</sub> and COF<sub>A+D</sub>, respectively. However, it is worth noting that the broader light-responsive range and enhanced light-harvesting ability play roles but are not the determinants for the prominent photocatalytic performance. In order to further determine the band structures of the polymers and their thermodynamic driving force for contaminants degradation, the valence band X-ray photoelectron spectroscopy (VB XPS) was employed (Fig. 4b). The valence band (VB) edges of COF<sub>A+B</sub>, COF<sub>A+C</sub> and COF<sub>A+D</sub> are located at 2.11, 2.16 and 2.29 eV, respectively. By using the equation of E<sub>CB</sub> = E<sub>VB</sub> - E<sub>g</sub>, their corresponding conduction band (CB) potentials are calculated to be -0.38, -0.40 and 0.08 eV, respectively. The energy band structures of these three photocatalysts are given in Fig. 4c. Derived from Mott–Schottky plot (Fig. S14), the flat-band potential of COF<sub>A+D</sub> is about 0.10 V (vs NHE). Therefore, we found that the CB edge potential of COF<sub>A+D</sub> is more positive than the standard redox potential E°(O<sub>2</sub>/O<sub>2</sub><sup>-</sup>) (-0.33 V<sub>NHE</sub>) and the excess electrons on COF<sub>A+D</sub> cannot reduce the molecular oxygen to O<sub>2</sub><sup>-</sup> species. This could be the fundamental cause that COF<sub>A+D</sub> polymer is incapable of photocatalytic degradation.

For the three COFs, hexagonal cluster models (Fig. S15) consisting of six precursors are selected as the target of theoretical calculations at density functional theory (DFT) level [23,24]. Previous results have shown that such type of hexagonal cluster could be representative semi-extended model for the COFs [9]. Thus the calculated results on these clusters could provide useful insights into the electronic structure of the COFs synthesized here.

In the theoretical calculation of solid materials based on cluster model, the highest occupied molecular orbital (HOMO) and the lowest unoccupied molecular orbital (LUMO) are usually considered as the counterparts of VB and CB levels. The HOMO-LUMO gap in the cluster model could be used to estimate the band gap of actual solid materials theoretically. The HOMO-LUMO gaps from all the hybrid functionals correctly reproduce the trend of variation of experimental band gaps among the COFs here (Table S5 and Fig. S16). This result implies the reliability of the calculated results. The clear separations between HOMO and LUMO exist for the model structures of all the COFs here (Figs. S17 and S18), implying that well separation between the photo-generated charge carriers is probable.

It should be mentioned that, description solely based on orbitals, which are not observable, could be highly difficult and thus alternative descriptors on the photocatalytic activity should be explored [9]. As shown before, one important possible intermediate in the photocatalytic process is the radical anion formed from the binding of one extra electron by the COFs. The stability of the radical anion would have significant impact on the photocatalytic activity of the COFs. As shown in Fig. S19, all the theoretical results demonstrate that COF<sub>A+C</sub> attains the largest electron affinity (EA) among the three COFs. Therefore, it is highly probable that the photocatalytic process of this COF takes place via the most stable reaction intermediate and thus COF<sub>A+C</sub> possesses the highest photocatalytic activity. Furthermore, the EA of COF<sub>A+D</sub> is the smallest which is also consistent with the fact that the activity of this COF as photocatalyst is the poorest here.

The efficient generation, migration, and separation of photoinduced electron-hole pairs are prerequisite to initiate photocatalysis, which can

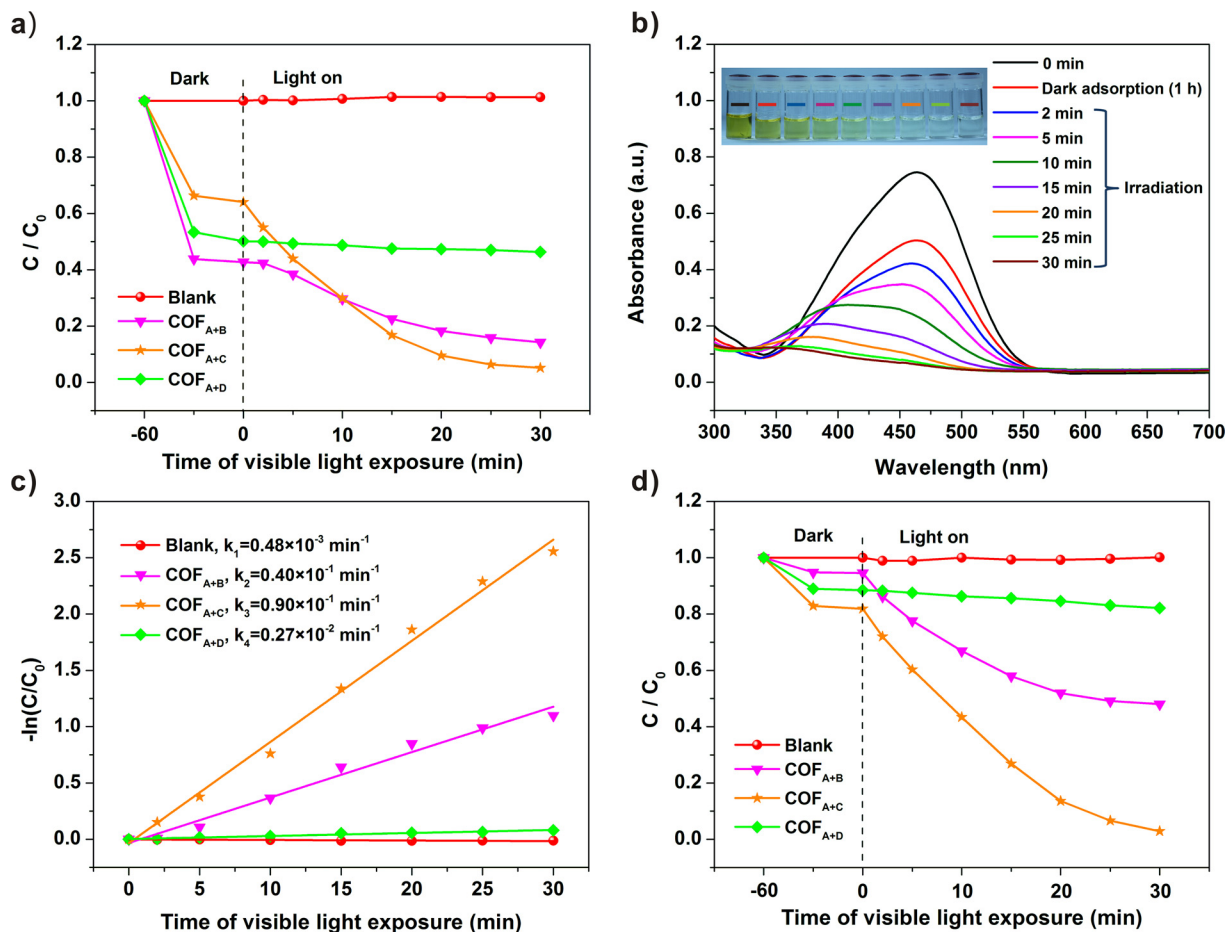


**Fig. 3.** (a) Photocatalytic degradation of MO (10 mg L<sup>-1</sup>) over COF<sub>A+B</sub>, COF<sub>A+C</sub> and COF<sub>A+D</sub> under visible light irradiation; (b) UV-vis absorption spectra of MO under different irradiation times by using COF<sub>A+C</sub>; (c) kinetics linear simulation curves of MO photodegradation over different photocatalysts and the inset is the value of the rate constant  $k$ ; (d) photocatalytic degradation of phenol (10 mg L<sup>-1</sup>) over COF<sub>A+B</sub>, COF<sub>A+C</sub> and COF<sub>A+D</sub> under visible light irradiation. (For interpretation of the references to color in the text, the reader is referred to the web version of this article).

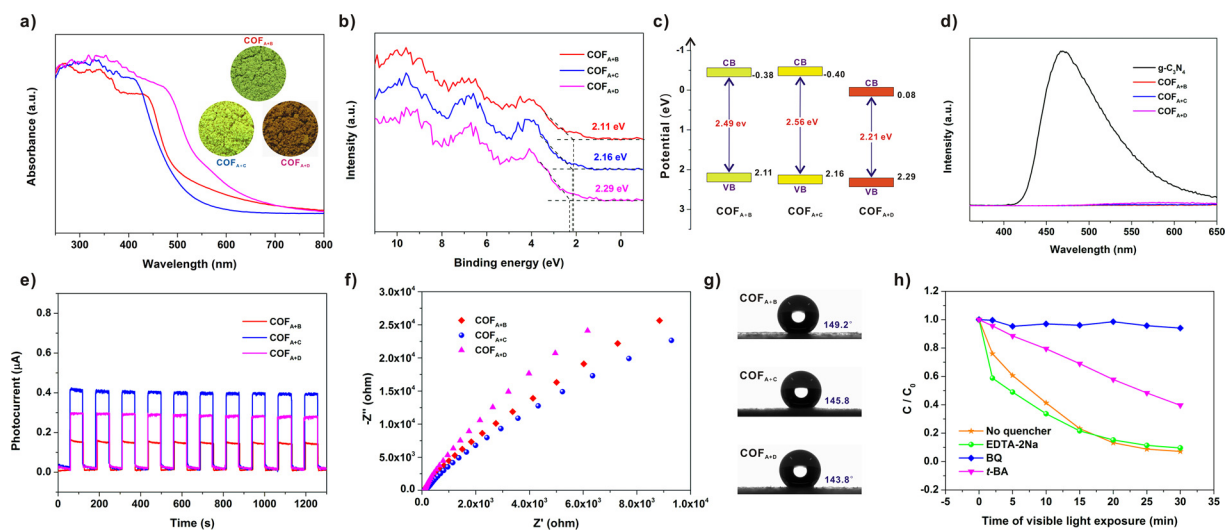


**Fig. 4.** (a) UV-vis diffuse reflectance spectra, (b) VB XPS spectra, (c) band alignment, (d) photoluminescence spectra, (e) photocurrent responses, (f) EIS Nyquist plots, (g) water contact angle measurements of COF<sub>A+B</sub>, COF<sub>A+C</sub> and COF<sub>A+D</sub>; (h) photodegradation of MO over COF<sub>A+C</sub> with different scavengers, C<sub>0</sub> is the initial concentration of MO after dark adsorption tests.

be analyzed by photoluminescence (PL) spectroscopy, photocurrent response, and electrochemical impedance spectroscopy (EIS). PL emission spectra originating from the recombination of free charge carriers were applied to disclose the photoinduced interfacial charge dynamics

of semiconductors. The lower PL intensity corresponds to the higher separation efficiency of photogenerated electron-hole pairs. Obviously, the PL emissions of three COFs were fully quenched in comparison with the pristine g-C<sub>3</sub>N<sub>4</sub> (Fig. 4d), indicating that the π-conjugated backbone

and inherent porosity of COFs could effectively promote charge transfer and separation upon photoexcitation. The transient photocurrent responses of  $\text{COF}_{\text{A}+\text{B}}$ ,  $\text{COF}_{\text{A}+\text{C}}$  and  $\text{COF}_{\text{A}+\text{D}}$  with several on-off cycles of intermittent visible light irradiation were compared in Fig. 4e, revealing that  $\text{COF}_{\text{A}+\text{C}}$  has the highest photocurrent intensity among the three samples. This confirms that more visible-light active centers in the polymer structure facilitate the generation of photoexcited charge carriers, and the extend conjugation by aromatic rings incorporation improves the carrier mobility. And the photocurrents of these polymers are steady and recyclable. Furthermore, the arc radius of  $\text{COF}_{\text{A}+\text{C}}$  on EIS Nyquist plot is smaller than those of  $\text{COF}_{\text{A}+\text{B}}$  and  $\text{COF}_{\text{A}+\text{D}}$  (Fig. 4f), consistent with the corresponding photocatalytic degradation activities. In contrast to  $\text{COF}_{\text{A}+\text{B}}$ , the interdigitated triazine-benzene heterojunctions in  $\text{COF}_{\text{A}+\text{C}}$  could decrease the probability of electron-hole recombination. In the case of  $\text{COF}_{\text{A}+\text{D}}$ , the group of hydrazine in its networks certainly breaks the  $\pi$ -delocalized electronic system, thereby leading to reduced electron-transfer conductivity and inhibited interfacial charge transfer. In brief, for  $\text{COF}_{\text{A}+\text{C}}$  photocatalyst, the greater density of photocatalytic active sites and the higher conjugation degree within its framework are more favorable for photocatalysis.

The surface properties of these three polymers were also explored by contact angle measurements. As seen in Fig. 4g,  $\text{COF}_{\text{A}+\text{B}}$ ,  $\text{COF}_{\text{A}+\text{C}}$  and  $\text{COF}_{\text{A}+\text{D}}$  are hydrophobic (water contact angles were  $149.2^\circ$ ,  $145.8^\circ$  and  $143.8^\circ$ , respectively), and their surface hydrophobicity decreased slightly with increasing nitrogen content in the frameworks. As the better hydrophilic property of photocatalyst could promote water adsorption and subsequent reactive oxygen species formation, we speculated that the photocatalytic capacity will be strengthened by predesign the chemical structure of polymer to improve its hydrophilicity. The molecular skeleton of polymer determines its physicochemical properties, and all these properties collectively impact its photocatalytic performance. Therefore, by rational designing organic building units to construct diverse COFs with different structural configurations, we could render photocatalyst desired features for further photocatalytic application.

To elucidate the photocatalytic mechanism of  $\text{COF}_{\text{A}+\text{C}}$ , the radical trapping experiments were performed to study the roles of possible active species in photocatalysis by adding several chemicals, that is, *tert*-butanol (*t*BA, a hydroxyl radical scavenger), *p*-benzoquinone (BQ, a superoxide radical scavenger), and ethylenediaminetetraacetic acid disodium salt (EDTA-2Na, a hole scavenger), respectively. As evident from Fig. 4h, the MO decomposition is completely restrained by the addition of BQ, whereas the photocatalytic degradation efficiency of MO is slightly reduced in the presence of *t*BA. Conversely, the MO photodegradation kinetics is accelerated with the existence of EDTA-2Na. This demonstrates that the competitive reaction of excess holes with EDTA-2Na decreases the electron-hole recombination, leading to more available electrons for oxidative radical-mediated degradation [25]. All these results suggest that the photodegradation of organic pollutants is driven by the main contribution of superoxide radicals ( $\text{O}_2^{\cdot-}$ ) with the assistance of hydroxyl radicals ( $\text{OH}^{\cdot}$ ).

On the basis of the analyses and discussions above, the underlying photocatalytic mechanism of  $\text{COF}_{\text{A}+\text{C}}$  is proposed as illustrated in Fig. 5. When  $\text{COF}_{\text{A}+\text{C}}$  is excited with photons of energy exceeding (or equal to) the bandgap, photoinduced electrons are injected into the CB, thus resulting in the electrons and holes separating and escaping recombination. Subsequently, the accumulated electrons in the CB are trapped by the dissolved  $\text{O}_2$  to yield abundant  $\text{O}_2^{\cdot-}$  radicals, which further react with  $\text{H}_2\text{O}$  to form  $\text{OH}^{\cdot}$  radicals; while holes can easily spread out over polymer system to catch pollutants or oxide water, leading to effective spatial charge separation. Eventually, these generated highly oxidative species ( $\text{O}_2^{\cdot-}$  and  $\text{OH}^{\cdot}$  radicals) can efficiently degrade and mineralize organic pollutants.

In addition to the photocatalytic activity, the durability and stability of the photocatalyst is also crucial for practical applications. Herein, the recycling tests were carried out to investigate the stability of

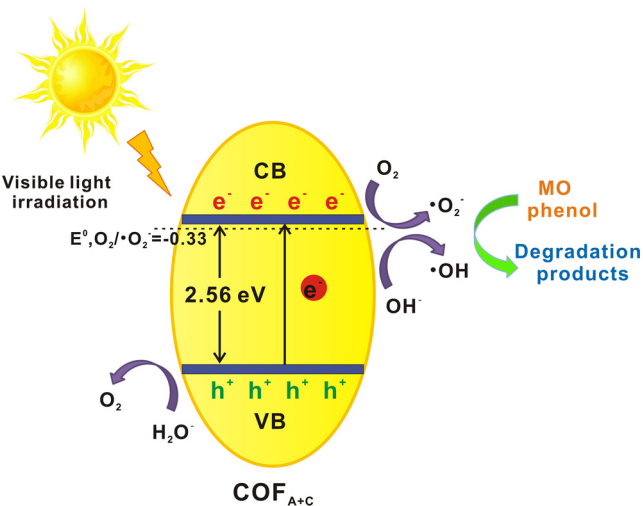


Fig. 5. A schematic illustration of pollutants photodegradation over  $\text{COF}_{\text{A}+\text{C}}$  under visible light irradiation.

synthesized photocatalysts via the degradation of MO and phenol under visible light illumination, and the results are shown in Fig. S20. Impressively, the photocatalytic abilities of  $\text{COF}_{\text{A}+\text{B}}$  and  $\text{COF}_{\text{A}+\text{C}}$  were retained at over 80% of their original values even after recycling four times. This indicated that these COFs can be effectively reused for repeated photocatalytic cycles without any major loss of their activities. Furthermore, no noticeable changes have been observed, either in the morphology or in the chemical structure of  $\text{COF}_{\text{A}+\text{C}}$  after the dye photodecomposition, as further proved by TEM and FT-IR spectra (Figs. S21 and S22). The remarkable stabilities of these photocatalysts stem from their intrinsic chemical structures, which are constructed with organic building units through robust covalent bonds.

#### 4. Conclusion

In summary, a series of imine-bond linked COFs with photocatalytic active center inlaid were designed and synthesized, and the intrinsic advantages of COFs, namely crystallinity, porosity and tunability, were successfully merged into photocatalytic system. Subsequently, the photoelectric properties and photocatalytic performance of the three COFs were systematically investigated and compared. The results demonstrate that steric and electronic variations in the monomers were transferred to the resultant COFs, which allow their band structures and physical properties to modulate depending on the density of active centers and the conjugation degree. Through rational band gap and photocatalytic site engineering by tailoring the rigid molecular precursors,  $\text{COF}_{\text{A}+\text{C}}$  exhibited superior visible light photocatalytic activity and stability for water purification. Therefore, we believe that this strategy not only contributes to a better understanding of the structure–property relationship of COFs for photocatalysis, but also could gain the molecular design principles to guide future preparation of high-performance photocatalyst.

#### Acknowledgments

This work was supported by the National Key Research and Development Program (2016YFA0203102), the National Natural Science Foundation of China (21537004, 21477140, 21621064, 21777169), and the Strategic Priority Research Program of the Chinese Academy of Sciences (XDB14010201).

#### Appendix A. Supplementary data

Supplementary material related to this article can be found, in the

online version, at doi:<https://doi.org/10.1016/j.apcatb.2018.08.005>.

## References

- [1] S.-Y. Ding, W. Wang, Covalent organic frameworks (COFs): from design to applications, *Chem. Soc. Rev.* 42 (2013) 548–568.
- [2] X. Feng, X. Ding, D. Jiang, Covalent organic frameworks, *Chem. Soc. Rev.* 41 (2012) 6010–6022.
- [3] J.L. Segura, M.J. Mancheño, F. Zamora, Covalent organic frameworks based on schiff-base chemistry: synthesis, properties and potential applications, *Chem. Soc. Rev.* 45 (2016) 5635–5671.
- [4] J.W. Colson, W.R. Dichtel, Rationally synthesized two-dimensional polymers, *Nat. Chem.* 5 (2013) 453–465.
- [5] C.J. Doonan, D.J. Tranchemontagne, T.G. Glover, J.R. Hunt, O.M. Yaghi, Exceptional ammonia uptake by a covalent organic framework, *Nat. Chem.* 2 (2010) 235–238.
- [6] S. Das, P. Heasman, T. Ben, S. Qiu, Porous organic materials: strategic design and structure–function correlation, *Chem. Rev.* 117 (2017) 1515–1563.
- [7] F. Ding, D. Yang, Z. Tong, Y. Nan, Y. Wang, X. Zou, Z. Jiang, Graphitic carbon nitride-based nanocomposites as visible-light driven photocatalysts for environmental purification, *Environ. Sci.: Nano* 4 (2017) 1455–1469.
- [8] J. Zhang, Y. Wu, M. Xing, S.A.K. Leghari, S. Sajjad, Development of modified N doped TiO<sub>2</sub> photocatalyst with metals, nonmetals and metal oxides, *Energy Environ. Sci.* 3 (2010) 715–726.
- [9] V.S. Vyas, F. Haase, L. Stegbauer, G. Savasci, F. Podjaski, C. Ochsenfeld, B.V. Lotsch, A tunable azine covalent organic framework platform for visible light-induced hydrogen generation, *Nat. Commun.* 6 (2015) 8508.
- [10] L. Stegbauer, K. Schwinghammer, B.V. Lotsch, A hydrazone-based covalent organic framework for photocatalytic hydrogen production, *Chem. Sci.* 5 (2014) 2789–2793.
- [11] X. Jiang, P. Wang, J. Zhao, 2D covalent triazine framework: a new class of organic photocatalyst for water splitting, *J. Mater. Chem. A* 3 (2015) 7750–7758.
- [12] S. Jin, X. Ding, X. Feng, M. Supur, K. Furukawa, S. Takahashi, M. Addicoat, M.E. El-Khouly, T. Nakamura, S. Irle, S. Fukazumi, A. Nagai, D. Jiang, Charge dynamics in a donor–acceptor covalent organic framework with periodically ordered bicontinuous heterojunctions, *Angew. Chem. Int. Ed.* 52 (2013) 2017–2021.
- [13] S. He, Q. Rong, H. Niu, Y. Cai, Construction of a superior visible-light-driven photocatalyst based on a C<sub>3</sub>N<sub>4</sub> active centre–photoelectron shift platform–electron withdrawing unit triadic structure covalent organic framework, *Chem. Commun.* 53 (2017) 9636–9639.
- [14] W. Tu, Y. Xu, J. Wang, B. Zhang, T. Zhou, S. Yin, S. Wu, C. Li, Y. Huang, Y. Zhou, Z. Zou, J. Robertson, M. Kraft, R. Xu, Investigating the role of tunable nitrogen vacancies in graphitic carbon nitride nanosheets for efficient visible-light-driven H<sub>2</sub> evolution and CO<sub>2</sub> reduction, *ACS Sustain. Chem. Eng.* 5 (2017) 7260–7268.
- [15] R.S. Sprick, J.-X. Jiang, B. Bonillo, S. Ren, T. Ratvijitvech, P. Guiglion, M.A. Zwijnenburg, D.J. Adams, A.I. Cooper, Tunable organic photocatalysts for visible-light-driven hydrogen evolution, *J. Am. Chem. Soc.* 137 (2015) 3265–3270.
- [16] S. Yang, D. Prendergast, J.B. Neaton, Tuning semiconductor band edge energies for solar photocatalysis via surface ligand passivation, *Nano Lett.* 12 (2012) 383–388.
- [17] H. Kisch, H. Weiß, Tuning photoelectrochemical and photocatalytic properties through electronic semiconductor–support interaction, *Adv. Funct. Mater.* 12 (2002) 483–488.
- [18] X. Ji, X. Yuan, J. Wu, L. Yu, H. Guo, H. Wang, H. Zhang, D. Yu, Y. Zhao, Tuning the photocatalytic activity of graphitic carbon nitride by plasma-based surface modification, *ACS Appl. Mater. Interfaces* 9 (2017) 24616–24624.
- [19] S. Zuluaga, L.-H. Liu, N. Shafiq, S.M. Rupich, J.-F. Veyan, Y.J. Chabal, T. Thonhauser, Structural band-gap tuning in g-C<sub>3</sub>N<sub>4</sub>, *Phys. Chem. Chem. Phys.* 17 (2015) 957–962.
- [20] J. Ran, T.Y. Ma, G. Gao, X.-W. Du, S.Z. Qiao, Porous p-doped graphitic carbon nitride nanosheets for synergistically enhanced visible-light photocatalytic H<sub>2</sub> production, *Energy Environ. Sci.* 8 (2015) 3708–3717.
- [21] A. Nagai, X. Chen, X. Feng, X. Ding, Z. Guo, D. Jiang, A squaraine-linked mesoporous covalent organic framework, *Angew. Chem. Int. Ed.* 52 (2013) 3770–3774.
- [22] Q. Liang, Z. Li, Z.-H. Huang, F. Kang, Q.-H. Yang, Holey graphitic carbon nitride nanosheets with carbon vacancies for highly improved photocatalytic hydrogen production, *Adv. Funct. Mater.* 25 (2015) 6885–6892.
- [23] R.G. Parr, W. Yang, *Density Functional Theory of Atoms and Molecules*, Oxford University Press, New York, 1989.
- [24] W. Koch, M.C. Holthausen, *A Chemist's Guide to Density Functional Theory*, Wiley, Weinheim, 2000.
- [25] S. Ghosh, N.A. Kouamé, L. Ramos, S. Remita, A. Dazzi, A. Deniset-Besseau, P. Beaunier, F. Goubard, P.-H. Aubert, H. Remita, Conducting polymer nanostructures for photocatalysis under visible light, *Nat. Mater.* 14 (2015) 505–511.